Framework for integrated plant and control optimization of electro-thermal systems: an energy storage system case study

Cary Laird[a], Ziliang Kang[b], Kai A. James[b], Andrew G. Alleyne[a,*]

[a] Mechanical Science and Engineering Department, University of Illinois at Urbana-Champaign, Urbana, IL 61801, USA
[b] Aerospace Engineering Department, University of Illinois at Urbana-Champaign, Urbana, IL 61801, USA

Keywords: hybrid energy storage, thermal energy storage, electrified vehicles

ABSTRACT

Advances in power density, energy storage technology, and thermal management are crucial to increased electrification of vehicles, especially those with high ramp rate loads. To meet these demands, a systems-minded design approach is needed, capable of simultaneously optimizing multi-domain system dynamics including control. This work provides a framework for simultaneous plant and control design leveraging a graph-based modeling tool for multi-domain dynamics. The graph-based modeling tool captures system-level dynamics spanning multiple energy domains. This tool facilitates control design by providing a state-space-like set of dynamic equations that describe the system's behavior and are computationally inexpensive to simulate. Modular, scalable graph-based models enable design optimization for both plant and controller design. To demonstrate an application of the framework, a hybrid electro-thermal energy storage system is described to provide a power-dense energy storage solution for classes of future electrified vehicles with high ramp rate power demands. Heuristic controllers protect energy storage elements while meeting reference signal commands. Sizing and control parameters of the energy storage system are optimized using the graph-based optimization framework. Simultaneous optimization of both components and control parameters demonstrate significant reductions in size while retaining a high level of performance, leading to improvements in power density.

NOMENCLATURE

Abbreviations

A	Advection
AC	Alternating current
CD	Conduction
CEP	Controlled electrical power
CP	Cold plate heat exchanger
CV	Convection
DC	Direct current
EP	Electrical power
HESS	Hybrid energy storage system
HETESS	Hybrid electro-thermal energy storage system

[*] Corresponding author.
Email addresses: caryel2@illinois.edu (C. Laird), kang134@illinois.edu (Z. Kang), alleyne@illinois.edu (A.G. Alleyne), kaijames@illinois.edu (K.A. James)

HRR	High ramp rate
HX	Heat exchanger
LHD	Load-haul-dump
LPF	Low pass filter
PCM	Phase change material
PI	Proportional-integral
PID	Proportional-integral-derivative
RL	Resistive losses
SOC	State of charge
TES	Thermal energy storage
TESS	Thermal energy storage system
UC	Ultracapacitor

Roman letters

C	Vertex capacitance (various)
$\boldsymbol{C}$	Capacitance matrix (-)
c_p	Specific heat (J kg^{-1} K^{-1})
$\boldsymbol{D}$	Source flow matrix (-)
E	Energy (J)
f	Mathematical formulation of power flow (-)
G, k	Constant multiplicative gain (-)
g	Nonlinear design constraint (-)
I	Current (A)
J	Cost function (-)
L	Inductance (H)
$\bar{\boldsymbol{M}}$	Incidence matrix (-)
$\dot{m}$	Mass flow rate (kg s^{-1})
m	Mass (kg)
N	Number of cells (-)
P	Power flow (W)
p	Power consumption (W)
q	Battery state of charge (-)
Q	Battery storage capacity (Ah)
R	Resistance (Ω)
s	Slack variable (various)
T	Temperature (C)
t	Time (s)
u	Actuator input (-)
U	Heat transfer coefficient (W K^{-1})
V	Voltage (V)
x	Vertex state (various)

Greek letters

α	Proportional control gain scaling variable
β	Integral control gain scaling variable
η	Efficiency
θ	Plant design variables
Λ	Weighting matrix
ϕ	Controller design variables
Ψ	Design matrix
ψ	Design variable scaling relationship

Subscripts

batt	Battery
i, j	Index
m	Melting
ocv	Open circuit voltage
p	Parallel
P	Power flow
perf	Performance
ref	Reference
s	Series
UC	Ultracapacitor
v	Valve

1. INTRODUCTION

With many countries and industries targeting net-zero greenhouse gas emissions in the next few decades [1], [2], emissions regulations have led to rapid growth of electrified vehicle industries. While electrification is most prevalent in the exponential growth in the number of battery electric automobiles since 2010 [3], other segments of the electrified mobility market, such as hybrid vehicles, light commercial vehicles, electric buses, construction vehicles, ships, and aircraft, have also experienced a marked increase. Energy storage technology is a key enabler towards the continued increase in electrification of vehicles. For electric vehicles to become ubiquitous in all mobility applications, advances in energy storage technology are necessary to increase power density [4]. This must be achieved by including high-performing systems in smaller packages, while mitigating thermal management challenges and safely providing transient power demands [5]–[7].

While battery energy storage offers a viable solution for most consumer electric vehicles, the relatively low power density of battery energy storage renders this technology non-optimal for city buses, heavy construction vehicles, mining vehicles, and other vehicles which experience high ramp rate (HRR) power demands. Additionally, HRR thermal loads resulting from these power demands present a challenge to traditional thermal management systems relying solely on liquid or air cooling [6]. This coupling between electrical and thermal domains makes it important for the design engineer to consider both domains in the design process. In the case of HRR loading, the ability to model and control transients in energy storage elements is paramount. Because of

these considerations, concepts of multi-domain optimization [8] and control co-design [9], [10] are suitable for designing an electro-thermal energy storage system.

As an alternative to battery-only electric energy storage, some vehicle systems employ hybrid electrical energy storage. Combining dissimilar storage elements, hybrid energy storage can offer improved overall performance [11]–[13]. Particularly, hybrids containing energy-dense battery cells and power-dense ultracapacitor cells are popular for HRR or pulsed loads, with ultracapacitors suitable for handling high peak demands and batteries capable of providing average power requirements [14]–[16]. Similarly, hybridized thermal management systems employing phase change thermal energy storage in traditional cooling systems have been considered as an efficient, lightweight cooling solution for HRR thermal loads [17] [18]. There are several studies considering optimal sizing of electrical energy storage elements within a hybrid electrical energy storage system [19]–[29], many of which also examine control optimization. On the other hand, far fewer studies consider design [30]–[34] and energy management optimization [18], [35]–[37] for thermal energy storage.

However, system-level optimization of these multi-domain systems, including control, has received little attention in the literature, especially in the context of electro-thermal energy storage. Some have considered design of electrical and thermal energy storage for building applications [38]–[40]. While several of these studies have considered aspects of design and control optimization, these studies consider the electro-thermal design optimization problem from a different perspective, neglecting existence of electro-thermal coupling by treating electrical and thermal storage as physically separate entities working together to lower electricity costs. Additionally, methods presented within these studies consider much longer dynamic timescales on the order of several hours, rather than the seconds- or sub-seconds-long timescales on which vehicle dynamics evolve. Consideration of combined electrical and thermal performance of a hybrid electro-thermal energy storage system for electrified mobility through design and control optimization is largely missing in the literature.

Since HRR loads described above can vary in different applications, a framework and set of tools for analysis of a broad variety of systems is needed to address this gap. This framework should be flexible enough to allow users to tailor it for their own application and use profiles. Additionally, the tool set should be modular and scalable to allow a wide variety of component representations and number of components depending on the target application. The contribution of this work is the development and deployment of such a framework using tools and techniques from graph-based modeling, control, and design optimization. To make the framework concrete, we utilize a case study in which the plant and controller of a hybrid electro-thermal energy storage system (HETESS) are optimized for a candidate example: a load-haul-dump (LHD) mining machine. Key contributions of this paper include:
- Formulation and demonstration of a general graph-based framework for multi-domain, multi-objective optimization *including controller design*;
- A candidate HETESS architecture, including multi-domain couplings, for illustration of framework steps;
- A numerical case study of the proposed approach demonstrating potential improvements in power density of energy storage systems by reducing component sizes while simultaneously maintaining high levels of system performance.

The outline of the work is as follows. For clarity of exposition, Section 2 begins with an introduction of a candidate system architecture. Section 3 summarizes the graph-based framework used in this work for modeling, control, and design optimization. Section 4 describes a case study

4

which demonstrates the results of plant and controller optimization on a candidate example introduced in Section 2. Section 5 concludes the paper and discusses directions for future work.

2. EXAMPLE SYSTEM

The framework discussed in Section 3 is generalizable to a wide range of system architectures encompassing multiple energy domains, including electrical, thermal, and mechanical. In particular, these tools are well suited for systems with significant coupling between energy domains. To give the reader a more concrete understanding of the types of systems that can be addressed using this framework, we begin by providing an example of a physical system for which the framework can be applied. This example system is a hybrid electro-thermal energy storage system. The particular architecture chosen for the electro-thermal system is well suited to meet power and energy demands of vehicle systems with HRR electrical and thermal loading, such as heavy construction and mining vehicles [41], [42]. Importantly, this candidate system includes couplings between electrical and thermal domains.

The electrical subsystem, referred to here as the hybrid energy storage system (HESS), contains a battery pack, ultracapacitor pack, and two DC-DC power converters which interface with a shared voltage bus, as shown in Figure 1. This HESS configuration, known as the parallel active topology [43], allows the control engineer to leverage power density of ultracapacitor cells and energy density of battery cells via independent control of the storage elements. Hybridization of electrical energy storage in this way allows ultracapacitor cells to account for high power requirements during transient loading conditions, while battery cells provide average energy demands of the load. Though the battery-ultracapacitor HESS is not unique to a particular battery chemistry, the case study presented herein focuses on lithium-ion batteries due to their high power density relative to other chemistries. The HESS powers an electronic load, such as an electric motor (denoted as M in Figure 1), which may exhibit high ramp rates.

The thermal subsystem, referred to hereafter as the thermal energy storage system (TESS), is a single-phase liquid coolant thermal management system with phase change material (PCM) thermal energy storage (TES) modules. The coolant loop contains a liquid-liquid heat exchanger (HX), fluid reservoir, pump, continuously variable valve, and three cold plate heat exchangers (CPs). In this example system, complexity of the TESS and its controller is limited: the coolant loop is configured such that only two flow paths are considered. CPs 1 and 3 are connected in series in one flow path and CP2 is connected in parallel on a separate flow path, such that thermal loads generated by the HESS and HRR load are isolated on different paths. The framework in Section 3 is generalizable to explore more complex architectures depending on the target application and its modularity facilitates such topology changes. Similar to the HESS, the TESS is also hybridized in the sense that it employs thermal energy storage and thermal management. Thermal energy storage occurs through a change of PCM phase, and thermal management is performed by the liquid loop which moves thermal energy between three TES modules and heat exchanger. Paralleling the hybridization of the HESS, TES modules quickly store thermal energy from HRR thermal loads, while the HX rejects thermal energy at a limited rate which is appropriate for average thermal loads.

Components of the HESS are placed in contact with TES modules, allowing electro-thermal coupling via conductive heat transfer between electronic components and TES modules. In turn, TES modules are placed in contact with CPs, allowing conductive heat transfer between TES modules and the CP wall. While this conductive heat transfer is bi-directional, thick arrows in Figure 1 depict a direction of conductive heat transfer defined as positive for modeling purposes.

Should this direction be reversed, such as to warm a cold battery, the structure would be preserved with a sign change on the heat flow. In addition to these thick arrows, the electrical components, TES modules, and CPs are shaded in different colors to illustrate how these components are connected. The selected configuration of HESS components and CPs allows electrical energy storage elements, which are generally more sensitive to temperature fluctuations, to be separated thermally from power converters, which are expected to undergo more significant temperature fluctuations.

The candidate system described in this section exhibits many challenging aspects of integrated systems that our framework is well-equipped to handle, including multiple energy domains, coupling between these domains, and components which require actuation (DC-DC converters, pumps, valves). Note that this architecture is not unique in the sense that components and configuration can be changed to achieve different capabilities. Though other architectures are not explored in this article, the benefit of the proposed framework and modeling tools to be introduced is the flexibility to represent a wide variety of component behaviors and configurations. The architecture to use for a specific application is a choice left to the designer. Having described one potential candidate architecture, Section 3 discusses the framework and tools used to perform control co-design.
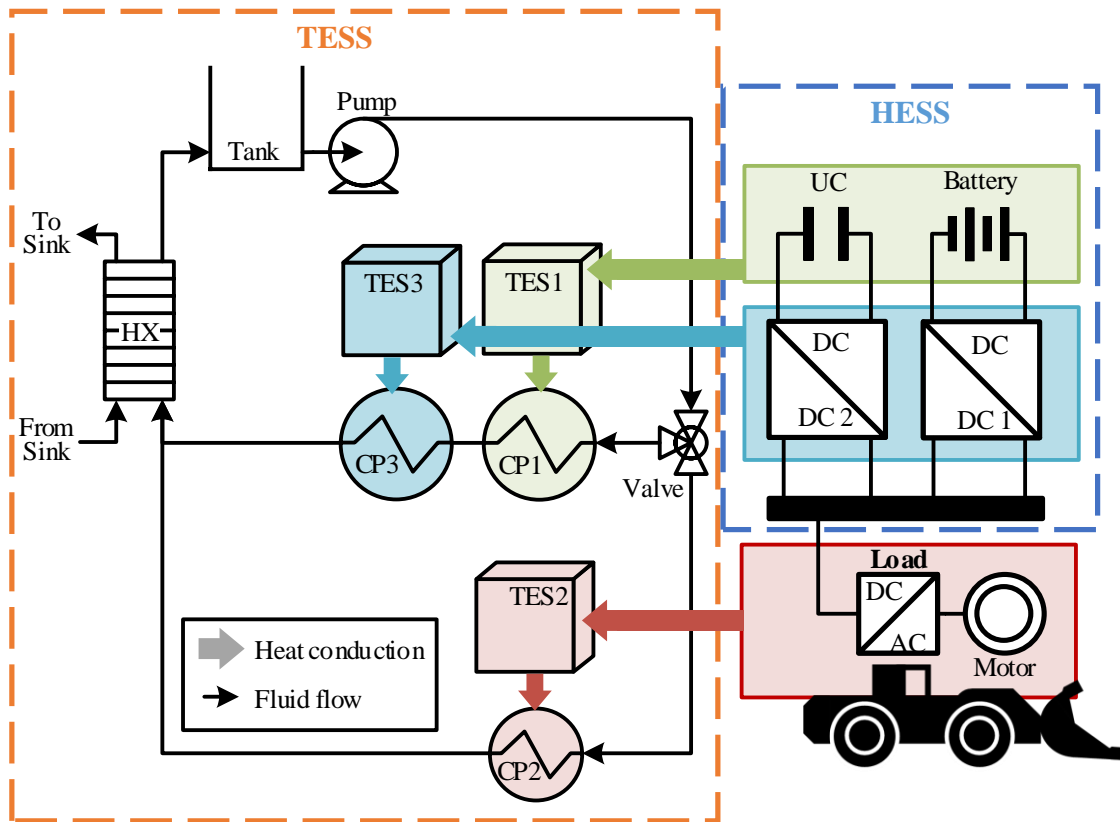

Figure 1: HETESS schematic.

3. GRAPH-BASED METHODS

The tools used in this work for modeling, control, and design optimization employ graph theoretic techniques to mathematically represent energy transfer within the HETESS and with its

environment. Merits of these tools include model modularity, scalability, computational efficiency, and a unique ability to encompass multiple energy domains in a unified framework [44]–[50]. Our framework, detailed in Figure 2, leverages these tools but also provides a user with flexibility to substitute their own processes for simulation, control design, and optimization formulation. To illustrate this flexibility, dashed lines indicate components of the framework that are up to a user to define. Solid lines indicate the fixed foundations of the framework that are essential to providing the benefits listed above. Namely, these foundations are the graph-based modeling and design optimization methods, together with the processes and features they enable. A brief introduction to the framework is provided here in the context of the HETESS and the interested reader is referred to the works cited above for more details.
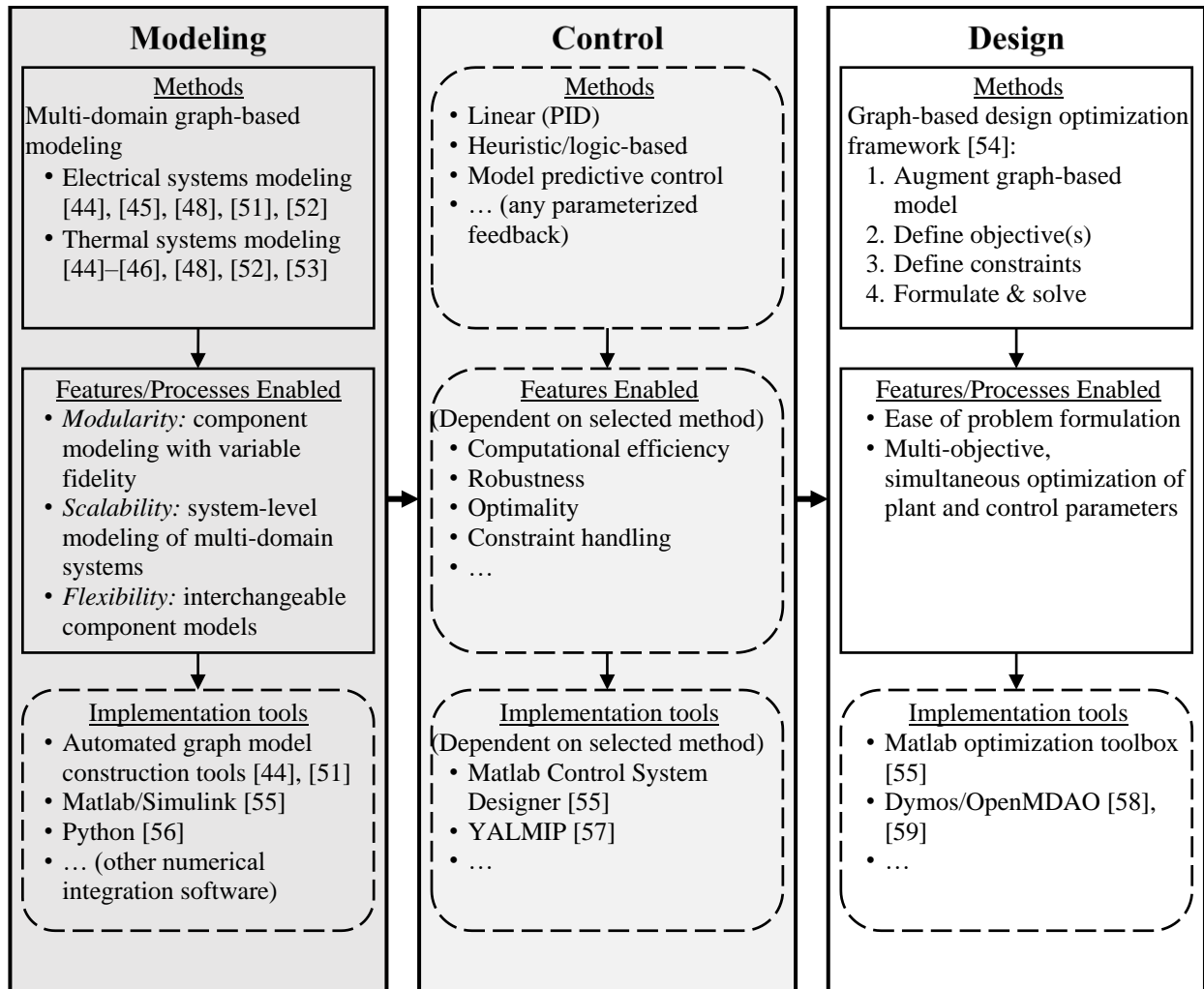
Modeling	Control	Design
Methods Multi-domain graph-based modeling • Electrical systems modeling [44], [45], [48], [51], [52] • Thermal systems modeling [44]–[46], [48], [52], [53]	**Methods** • Linear (PID) • Heuristic/logic-based • Model predictive control • … (any parameterized feedback)	**Methods** Graph-based design optimization framework [54]: 1. Augment graph-based model 2. Define objective(s) 3. Define constraints 4. Formulate & solve
Features/Processes Enabled • *Modularity:* component modeling with variable fidelity • *Scalability:* system-level modeling of multi-domain systems • *Flexibility:* interchangeable component models	**Features Enabled** (Dependent on selected method) • Computational efficiency • Robustness • Optimality • Constraint handling • …	**Features/Processes Enabled** • Ease of problem formulation • Multi-objective, simultaneous optimization of plant and control parameters
Implementation tools • Automated graph model construction tools [44], [51] • Matlab/Simulink [55] • Python [56] • … (other numerical integration software)	**Implementation tools** (Dependent on selected method) • Matlab Control System Designer [55] • YALMIP [57] • …	**Implementation tools** • Matlab optimization toolbox [55] • Dymos/OpenMDAO [58], [59] • …

Figure 2: System-level framework for modeling, control, and design of multi-domain electro-thermal systems.

3.1 Modeling

Power interactions and interconnections are represented as an oriented graph, where vertices each have corresponding state variables representing energy storage and oriented edges represent power transfers between states. Here, we distinguish between a directed and oriented

graph: the graphs utilized in this framework are oriented such that power can flow bi-directionally between vertices, where an edge's orientation indicates the assumed positive direction of power flow, whereas directed graphs would allow power to flow in a single direction along the edge. For instance, the assumed positive orientation of power flow associated with conductive heat flow discussed in Section 2 is reflected by the orientation of the corresponding edge. Associated with edge e_j is a bidirectional power transfer P_j (or power "flow"), which may be a nonlinear function of adjacent vertex states and an actuator input

$$P_j = f_j(x_j^{tail}, x_j^{head}, u_j), \tag{1}$$

where x_j^{tail} and x_j^{head} are tail and head vertex states of edge j. Applying conservation of energy to state x_i associated with vertex v_i yields the following state dynamic

$$C_i \dot{x}_i = P_i^{in} - P_i^{out} \tag{2}$$

where $C_i \geq 0$ is the vertex capacitance, and P_i^{in} and P_i^{out} are the sums of all power flows entering and leaving vertex i respectively. Repeating the calculation (2) for all states, the full system dynamics can be written as

$$C\dot{x} = -\bar{M}P + DP^s \tag{3}$$

where x is the state vector, C is a matrix of vertex capacitances, $\bar{M}$ maps edges to vertices, D maps external power flows to vertices, and P^s is a vector of external power flows. System-environment interactions are represented by external power flows and vertices, which are depicted with dashed outlines to visually differentiate from system vertices and edges.

The graph model representing electrical and thermal dynamics of the HETESS is shown in Figure 3. This graph contains vertices corresponding to battery state of charge (SOC), current, voltage, temperature, and PCM thermal energy storage states. States corresponding to each of these vertex types are denoted in the figure as q_i, I_i, V_i, T_i, and E_i, respectively. The capacitance C_i associated with each vertex varies depending on its type as specified in Table 1. There are six types of edges in this graph representing different mechanisms of power transfer: electrical power (EP), controlled electrical power (CEP), resistive losses (RL), advection (A), conduction (CD), and convection (CV). Power flows of the same type share similar governing equations, as given below:

$$P_{EP} = VI, \tag{4}$$

$$P_{CEP} = uVI, \tag{5}$$

$$P_{RL} = RI^2 \text{ or } V^2/R, \tag{6}$$

$$P_A = \dot{m}c_P T, \tag{7}$$

$$P_{CD/CV} = U(T^{tail} - T^{head}). \tag{8}$$

In (4)-(8), V represents voltage, I represents current, u is an actuator input, R is an electrical resistance, $\dot{m}$ is a mass flow rate, c_P is a fluid specific heat, T represents temperature, and U is an overall heat transfer coefficient for conduction or convection. The edge type corresponding to

8

each numbered edge is specified in Table 2. Combining the graph structure in Figure 3 with the information in Table 1 and Table 2, the nonlinear dynamic equations can be written in the form of (3). These six mechanisms of power transfer capture all relevant mechanisms for the example system considered in this work and can be used to model a wide variety of electrical and thermal components, including AC power electronics [51] and turbomachinery components [45] in addition to components considered here. Additional power transfer mechanisms can also be considered. For instance, previous works have modeled power transfers corresponding to linear and angular motion [52] and two-phase heat transfer [53].

The system graph model shown in the figure was obtained by combining component graph models for the battery pack, ultracapacitor pack, converters, bus, TES modules, CPs, HX, and tank. Component graph models used in this study are described at length in [54], and the process for combining these models into a system graph model amenable to simulation and control design is described in [44]. Detailed validation of component models used in the case study can be found in the literature as follows: Samsung 18650 lithium-ion battery pack and DC-DC converters [44]; Maxwell 100F ultracapacitor cell [16]; brazed-plate HX, pump, tank, and CP [46], [49]. The references all show a high degree of matching between the experimental modules and the modeled graph components and the reader is referred to these references for more detail and results. Moreover, the processes in [44], [54] provide users with an approach to customize the representation of their particular components or devices in the modeling framework presented here. While this work employs validated, low-order dynamic models of energy storage elements to maintain manageable computation times, these component models can readily be scaled up or down in complexity to achieve desired fidelity levels. For this work, a four-state graph model presented in [16] is reduced to a single state TES graph model to reduce computational complexity for the optimization routines. Validation of the single-state TES graph model is shown in Figure 4 by comparison with the average PCM temperature of experimental data presented in [55] and the average temperature of the four-state model [16]. This comparison was obtained for paraffin wax with a melting temperature of 52°C, heated at 315W for six hours then cooled by convection with ambient air at 19°C. Figure 4 illustrates that increased fidelity provides good agreement with experimental data, but the single-state model used in this work adequately captures nonlinear PCM behavior with lower computational expense. A notable advantage of the approach described here is its adaptability to add or exchange component models, which may have varying degrees of fidelity.
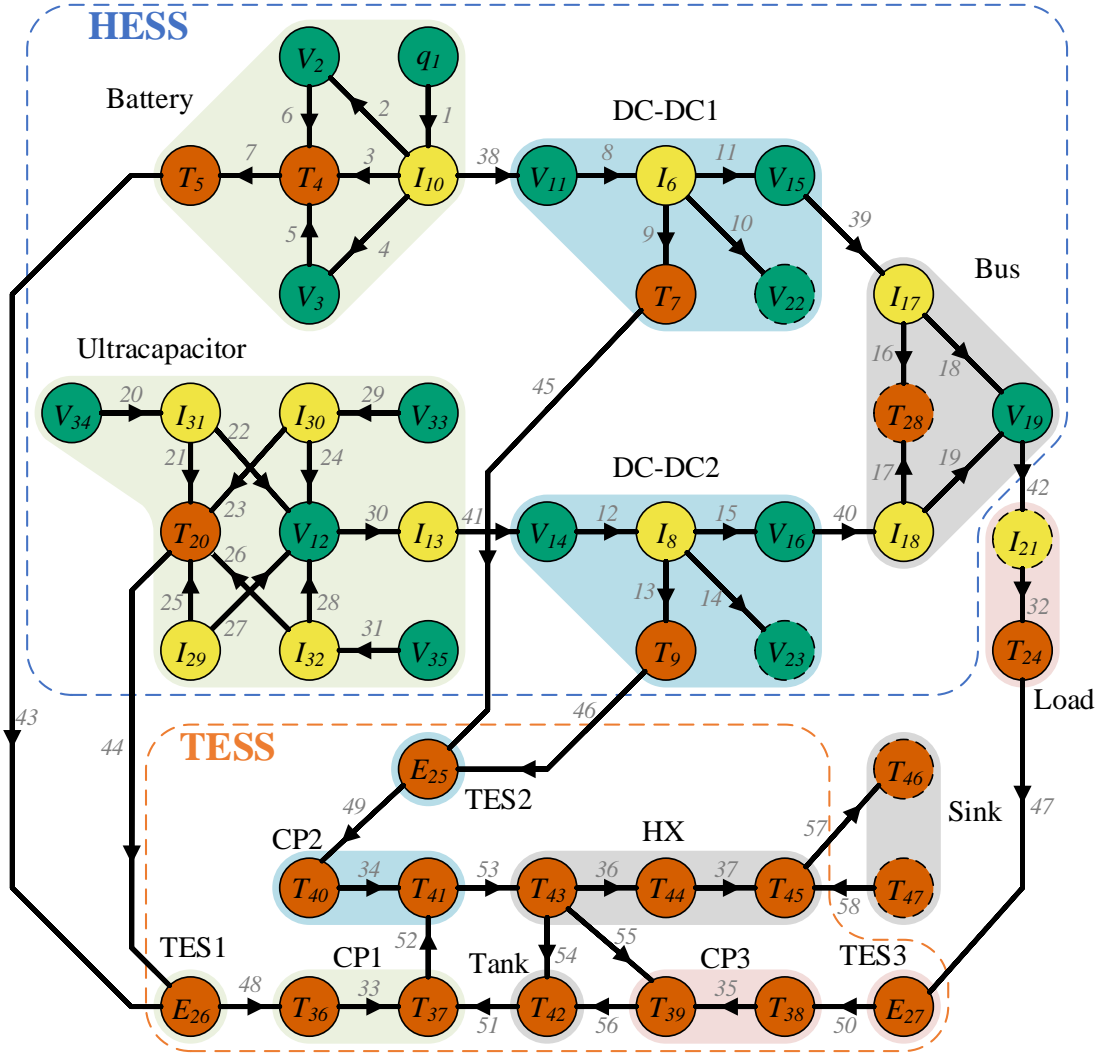
**Figure 3: HETESS graph model.**

Table 1: Vertex types and capacitances.

Description	State	Capacitance
Voltage	V	$C_V V$
Battery state of charge	q	$Q V_{ocv}(q)$
Current	I	LI
Temperature	T	C_T
PCM thermal energy storage	E	1

Table 2: Power flow edge equations by type.

Description (Type)	Edge Equation	Corresponding edge numbers
Electrical power (EP)[a]	$P_j = x_j^{tail} x_j^{head}$	1, 2, 4, 10, 11, 14, 15, 18, 19, 20, 22, 24, 27, 28-31, 38-42
Controlled electrical power (CEP)	$P_j = u_j x_j^{tail} x_j^{head}$	8, 12
Resistive losses (RL)	$P_j = k_j (x_j^{tail})^2$	3, 5, 6, 9, 13, 16, 17, 21, 23, 25, 26, 32
Advection (A)	$P_j = k_j u_j x_j^{tail}$	51-58
Conduction (CD)[b]	$P_j = k_j (T_j^{tail} - T_j^{head})$	7, 43-50
Convection (CV)	$P_j = k_j (x_j^{tail} - x_j^{head})$	33-37

[a]For edge 1, $x_j^{tail} = V_{ocv}(x_j^{tail})$, where V_{ocv} is battery open circuit voltage.

[b]For edges 43-50, TES module temperatures are functions of PCM thermal energy storage as in [54].
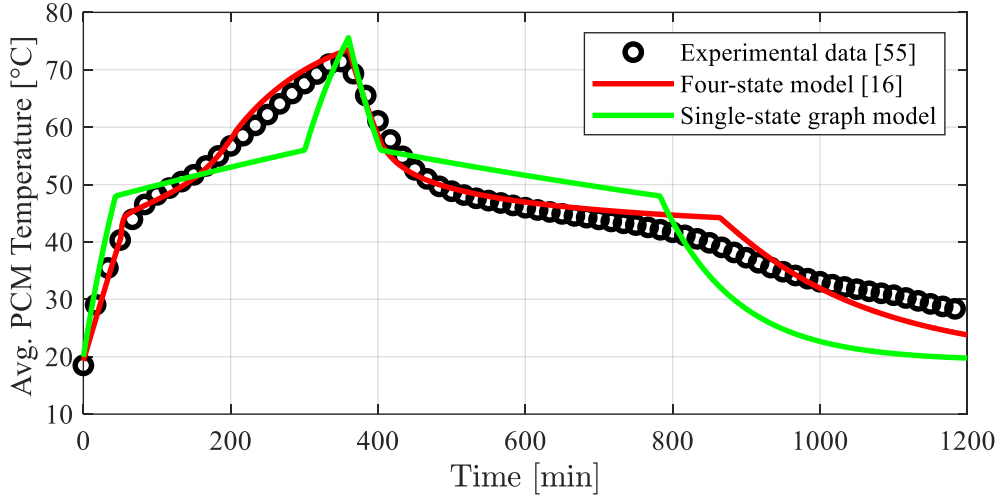
Figure 4: TES module model validation.

3. 2   Control

The graph-based framework used in this work is suitable for control design and has been used to develop several model-based controllers [44], [47], [50], [56]–[58]. Using the graph-based framework, the control design considered in this work employs heuristic controllers for electrical and thermal subsystems. Heuristic controllers are chosen for their computationally efficiency, resulting in a control co-design problem that can be solved with less computational expense as compared than one relying on optimization-based control. For the HESS, a filter-based method employing proportional-integral (PI) controllers, similar to that proposed in [59], is adopted to control the battery-ultracapacitor hybrid. For the TESS, a PI controller is developed which controls fluid temperatures through the TES modules by adjusting mass flow rates. The HESS and TESS controllers are introduced in this section. Demonstration of controller trajectories under nominal operation are provided as part of the case study in Section 4.

3.2.1 HESS Controller Design

Two control objectives for the HESS controller are protecting the battery from high discharge rates and maintaining bus voltage. To accomplish these objectives, two decoupled PI controllers are employed which dictate control inputs (duty cycles) for the DC-DC converters to meet these control objectives. The battery converter controller prevents the battery from supplying high discharge rates using a filter-based method. The electrical load power profile is passed through a low-pass filter (LPF) with a cutoff frequency smaller than the frequency of HRR load variations. For the case study in Section 4, the cutoff frequency is selected to be 0.0475Hz, which is around 30% smaller than the frequency of the load. The resulting signal is used as a reference for battery output power. Additionally, if losses are present in the HESS such that electrical efficiency can be estimated as a constant η, the battery power reference can be multiplied by a gain term $G = 1/\eta$ to ensure that the battery pack accounts for these losses. The ultracapacitor converter controller maintains bus voltage at a reference value. Because converter inputs are constrained to normalized values within [0,1], anti-windup strategies are necessary to mitigate integral windup in HESS controllers. In this work, a simple clamping strategy (also known as conditional integration) [60] is used to mitigate integral windup. Block diagrams for the described HESS controllers are provided in Figure 5.
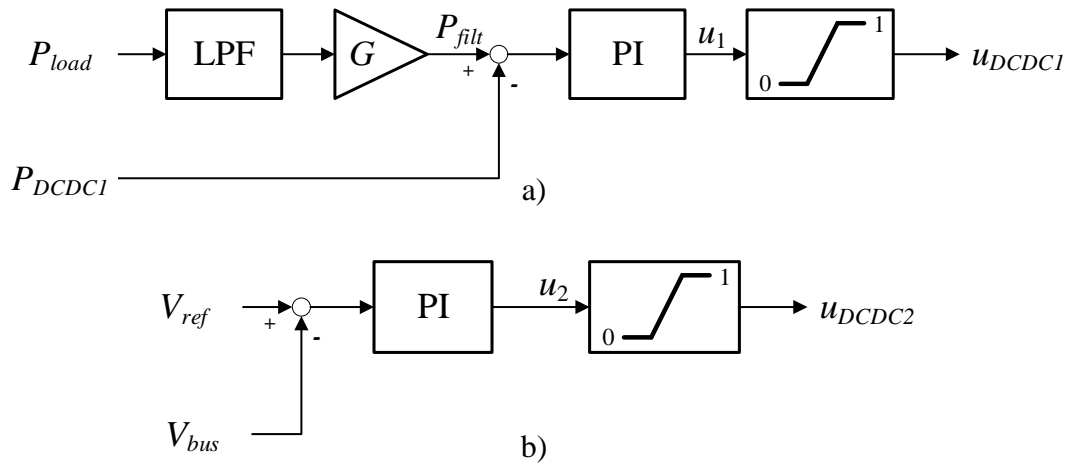

Figure 5: HESS controller block diagrams for a) battery converter and b) ultracapacitor converter.

3.2.2 TESS Controller Design

The objective for the TESS controller is to maintain fluid temperature through the CPs such that coolant remains colder than the melt temperature of the respective PCM. A secondary objective is to conserve energy. These are accomplished by varying mass flow rates through flow loops to vary the rate at which heat is absorbed from TES modules and subsequently rejected to sink fluid in the heat exchanger. Note that flow rates through the two flow loops are coupled in that their sum is the total mass flow rate in the system. The pump dictates this total flow rate, so its respective control design couples the temperature effects of the two flow sections. The valve setting is then chosen to proportion the total flow rate appropriately between the two flow sections.

12

The pump controller consists of two PI controllers corresponding to each of the two flow sections. One controller aims to regulate the temperature at the outlet of CP1 to a reference value, and the other aims to regulate the temperature at the outlet of CP2 to another reference value. These references are chosen to be 10°C below the melt temperature of the respective TES module. Each controller compares the actual temperature at the CP outlet to the respective reference temperature and applies PI control to the error between these two values. The two control signals are summed and the resulting signal is used as the duty cycle for the pump. Because the pump duty cycle input is constrained to lie within a normalized range of [0,0.65], anti-windup strategies are necessary to mitigate integral windup in the TESS controllers. In this work, a simple clamping strategy is used once more. The block diagram for the described pump controller is provided in Figure 6.
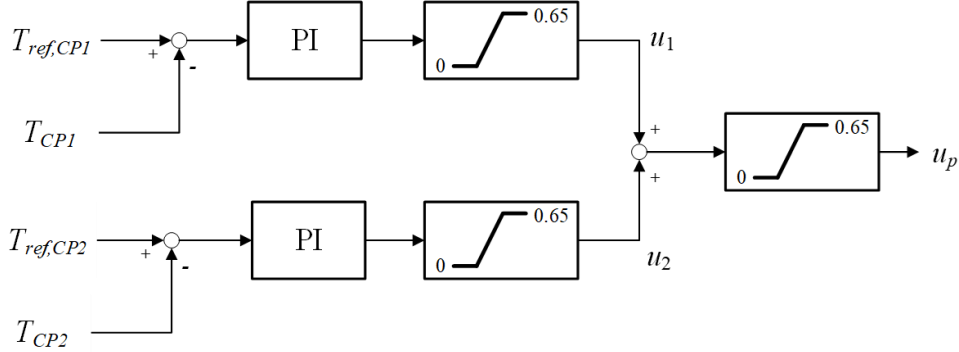
Figure 6: TESS pump controller block diagram.

With the pump dictating total flow rate through coolant loops, the solenoid valve proportions flow appropriately between the two flow sections. Its setting is defined according to

$$u_v = \frac{u_1}{u_1 + u_2},$$

(9)

where u_1 and u_2 are the saturated contributions of the two PI controllers and u_v is the valve setting. Mass flow rates through the two sections are then given by

$$\dot{m}_1 = u_v \dot{m}_{total},$$
$$\dot{m}_2 = (1 - u_v) \dot{m}_{total},$$

(10)

where $\dot{m}_1$ is flow rate through CP1, $\dot{m}_2$ is flow rate through CP2, and $\dot{m}_{total}$ is total mass flow rate. This choice of valve setting directs a larger portion of the total flow rate to travel through one of the CPs when its temperature exceeds its reference.

3.3 Design Optimization

In this work, a multi-objective optimization study is performed to minimize HETESS size while retaining high levels of performance. This is achieved by optimizing sizing and control performance of the HETESS as competing objectives. HESS sizing is determined by the number of battery cells in series and parallel, and the number of ultracapacitor cells in series and parallel. TESS sizing is determined by the mass and melt temperature of each of the PCMs in the TES

13

modules. Performance of both of these subsystems is dependent on these sizing variables as well as the controllers and their corresponding gains, so controller gains and sizing variables are optimized simultaneously. The full list of design variables, including plant variables θ and controller variables ϕ, considered in this study is provided below.

$$\theta = \{N_{p,batt}, N_{s,UC}, N_{p,UC}, m_1, T_{m1}, m_2, T_{m2}, m_3, T_{m3}\} \tag{11}$$

$$\phi = \{\alpha_1^{HESS}, \beta_1^{HESS}, \alpha_2^{HESS}, \beta_2^{HESS}, \alpha_1^{TESS}, \beta_1^{TESS}, \alpha_2^{TESS}, \beta_2^{TESS}\} \tag{12}$$

In (11), $N_{p,batt}$ is the number of parallel battery cells, $N_{s,UC}, N_{p,UC}$ are the numbers of series and parallel ultracapacitor cells respectively, m_i is the mass of the ith TES module, and $T_{m,i}$ is the melt temperature of the ith TES module. In (12), α_i^{HESS} and β_i^{HESS} correspond to gain scaling variables which are used to modify the proportional and integral gains, respectively, associated with the ith DC-DC converter. Similarly, α_i^{TESS} and β_i^{TESS} are gain scaling variables used to modify proportional and integral gains, respectively, associated with the ith CP. Note that the number of series battery cells may also be considered as a design variable, but in this study this parameter is held constant at a value chosen such that nominal pack voltage is slightly greater than the bus voltage setpoint. A variety of phase change materials may be considered for thermal energy storage modules, but in this work we focus on paraffin waxes. These PCMs are available commercially with a wide range of melt temperatures [61]–[63], so our treatment of PCM melt temperatures as design variables allows the designer to determine which melt temperatures are most appropriate for a given platform. Note that specific heat capacities of these PCMs are largely constant [61], [63] and as such are independent of melting temperature. However, consideration of other types of PCMs for which specific heat capacities are dependent on melting temperature can be accommodated using the graph-based framework. Additionally, note that the modularity of the framework allows users to readily swap component models of differing levels of fidelity if analysis deems it necessary. For instance, the TES module models used in this example can be replaced with higher-fidelity models without reformulating the entire system shown in Figure 3. Finally, note that several of these design variables physically correspond to integer values. However, because these variables are allowed to vary over a wide range of values, all design variables are treated as continuously variable here.

The following sections introduce design optimization for graph-based models as it pertains to the HETESS. This is based on a graph-based design optimization framework developed in [64] consisting of four steps: (i) augmenting the graph-based model with design matrices, (ii) defining design objectives, (iii) defining design constraints, and (iv) formulating and solving the optimization problem.

3.3.1 Augmenting the Graph-Based Model

A nominal graph-based model in the form of (3) can be augmented by introducing design matrices and operators that modify nominal values of graph elements (vertices, edges, and source edges). Design matrices scale nominal parameter values of graph elements according to the values of the design variables. A graph-based model which has been augmented with design matrices takes the form of

$$\Psi_c C\dot{x} = -\bar{M}\Psi P + D\Psi^s P^s \tag{13}$$

where Ψ_c, Ψ, and Ψ^s are diagonal design matrices of appropriate dimensions. In this equation, Ψ_c defines scaling relationships between design variables and vertex capacitances, Ψ defines scaling relationships for power flows, and Ψ^s defines scaling relationships for source power flows. The matrix Ψ_c is a diagonal matrix defined as follows

$$\Psi_c = \begin{bmatrix} \psi_{c,1}(\theta) & \cdots & 0 \\ \vdots & \ddots & \vdots \\ 0 & \cdots & \psi_{c,N_v}(\theta) \end{bmatrix} \tag{14}$$

where θ represents the set of continuous design variables and the function $\psi_{c,i}$ is defined in accordance with the underlying physics of the system to quantify the scaling relationship between the design variables and the capacitance of the ith vertex. For HETESS optimization, the Ψ_c design matrix captures effects of design variables on battery and ultracapacitor capacitances.

The remaining design matrices Ψ and Ψ^s in (13) are defined analogously for power flows and external power flows respectively. For HETESS optimization, the Ψ design matrix captures effects of the design variables on battery and ultracapacitor resistive losses and ultracapacitor power output. There are no external power flows in the HETESS graph model, so the Ψ^s matrix is the identity matrix. Additional design matrices are defined to account for elements of the closed-loop model not explicitly captured in (13), which include constraints and controller references. Scaling variables are used as design variables in this work to vary controller gain parameters from their nominal values. Design matrices are introduced to facilitate this scaling of nominal controller gains, which is key to achieving integrated plant *and control* optimization.

In the case that power flows are given by a nonlinear mapping of the design variables and state variables of adjacent vertices, elements of the graph model may not be modified appropriately by simple scaling relationships. In such cases, the nonlinear mappings of the design variables may be regenerated for each design. This is discussed in [54]. For HETESS optimization, this situation arises for power flows incident to PCM thermal energy storage vertices. Heat transfer terms associated with these power flows are functions of PCM temperatures, which are nonlinearly related to the design variables corresponding to PCM masses and melt temperatures.

3.3.2 Defining the Objective Function

The optimization cost function(s) vary for different applications, but may consist of combinations of static and dynamic costs. The goal of HETESS optimization is to minimize size while maximizing performance of the closed-loop system, which represents a multi-objective optimization problem. For this work, the optimization problem is formulated in the sense of minimization of a cost function. The sizing cost function (static) is taken as the total mass of electrical and thermal energy storage elements, given by

$$J_{size} = m_{batt} N_{p,batt} N_{s,batt} + m_{UC} N_{p,UC} N_{s,UC} + m_1 + m_2 + m_3, \tag{15}$$

where m_{batt} and m_{UC} are masses of battery cells and ultracapacitor cells respectively, $N_{p,batt}$ and $N_{s,batt}$ are the numbers of parallel and series battery cells respectively, $N_{p,UC}$ and $N_{s,UC}$ are the

15

numbers of parallel and series ultracapacitor cells respectively, and m_i is the mass of PCM in the ith TES module.

The HETESS control performance cost function is quantified by deviations from ideal closed-loop performance. It combines terms corresponding to state reference tracking, power flow reference tracking, state constraint violation, power flow constraint violation, and pump power consumption. The performance cost function (dynamic) is obtained by integrating its instantaneous value over the duration of the simulation. The instantaneous value of the performance cost function is given by

$$j_{perf}(t) = \| x(t) - x_{ref}(t) \|^2_{\Lambda_1} + \| P(t) - P_{ref}(t) \|^2_{\Lambda_2} + \| s(t) \|^2_{\Lambda_3} \\ + \| s_P(t) \|^2_{\Lambda_4} + \Lambda_5 p_{pump}(t)$$ (16)

where Λ_i is a weighting matrix for the ith term. In (16), the first and second terms correspond to reference tracking error for bus voltage and battery output power respectively. The third and fourth terms contain slack variables $s(t)$ and $s_P(t)$ which quantify amounts by which the states and power flows exceed their constraints. The third term corresponds to state constraint violations for temperatures and PCM states of charge. The fourth term corresponds to power flow constraint violations for battery output power, where bounds on output power are dependent on the design variable corresponding to the number of parallel battery cells. Note that (16) uses the notation $\|x\|^2_A = x'Ax$. The final term is instantaneous pump power consumption, which is determined as an empirical function of pump duty cycle and power transferred to the coolant. The performance cost function is obtained by integrating (16)

$$J_{perf} = \int_0^{t_{final}} j_{perf}(t)dt .$$ (17)

3.3.3 Defining the Design Constraints

Upper and lower bounds on the design variables can be defined by the design engineer to enforce any problem-specific limitations to which the design variables are subjected. Design constraints are defined as

$$\underline{\theta} \leq \theta \leq \overline{\theta} ,$$ (18)

$$\underline{\phi} \leq \phi \leq \overline{\phi} ,$$ (19)

$$g(\theta) \leq 0,$$ (20)

where $\underline{\theta}$ and $\overline{\theta}$ are lower and upper bounds of plant design variables respectively, $\underline{\phi}$ and $\overline{\phi}$ are lower and upper bounds of controller design variables respectively, and $g(\theta)$ defines any nonlinear constraints [64] acting on plant design variables. For the case study in Section 4, nonlinear constraints are not considered. Upper and lower bounds applied to HETESS design

variables for the case study are given in Table 3. Bounds on numbers of cells of electrical storage elements are chosen to prevent the HETESS from growing prohibitively large in mass, and to ensure the HETESS contains at least one cell of each storage element. Bounds on PCM mass are chosen similarly. PCM melt temperature constraints are chosen in accordance with the range of commercially available paraffin waxes. Controller gain scaling variables are constrained conservatively to maintain controller stability.

Table 3: Design variable constraints employed in case study.

Design Variable	Lower Bound	Upper Bound
Battery parallel cells	1	100
UC series cells	1	1000
UC parallel cells	1	100
Mass of PCMs 1-3 [kg]	0.25	50
Melt temperatures of PCMs 1-3 [°C]	31	80
Controller gain scaling variables	0.1	10

Definition of the cost function and constraints are integral, generalizable steps of the overall framework proposed in Figure 2. To make the framework concrete, we provide cost functions and constraints here that are relevant for the case study presented in Section 4.

3.3.4 Formulating and Solving the Optimization Problem

The final step in the framework is to formulate and solve the optimization problem. The optimization problem can be formulated using results from the preceding framework steps, as

$$\min_{\theta}\{J_{size}(\theta), J_{perf}(\theta,\phi)\} \tag{21}$$

$$\text{subject to}: \quad \Psi_c C\dot{x} = -\bar{M}\Psi P + D\Psi^s P^s$$
$$\underline{\theta} \leq \theta \leq \bar{\theta}$$
$$\underline{\phi} \leq \phi \leq \bar{\phi} \tag{22}$$

One solution tool for problems such as the described HETESS optimization, whose objective functions rely on dynamic simulations, utilizes the shooting method [65] to solve systems of dynamic and algebraic equations such as (13). For the HETESS optimization study considered here, this process consists of generating an augmented graph-based model for the current set of design variable values, then simulating the model under these conditions, and finally using the simulation results to calculate cost functions. Similar to the process described in [66], this solution method is shown in Figure 7. Note, the experienced user can substitute the method in Figure 7 for their preferred process.
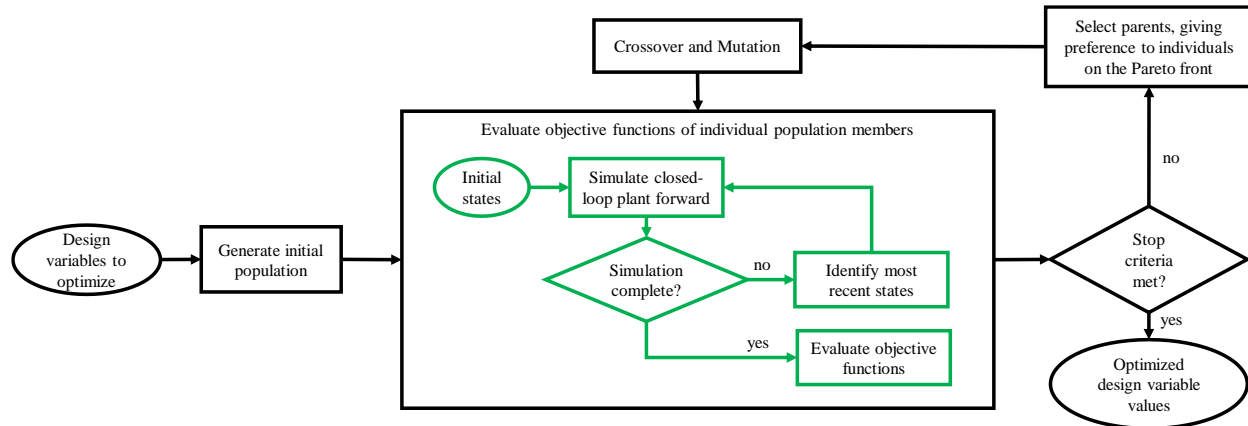
Figure 7: Flowchart of design optimization process using simulation model (green outline) and multi-objective genetic algorithm (black outline). Adapted from [66]**.**

4. CASE STUDY

The framework for modeling, control, and design optimization has been outlined in Section 3. To demonstrate the value of performing integrated plant and controller optimization using this framework, this section discusses implementation of the framework using the specific example introduced in Section 2. A case study was performed in which the HETESS optimization problem described above was solved for the case of an LHD mining machine. These machines encounter intermittent periods of high power demands during normal loading operations. The particular load profile applied to the HETESS in this work, derived from data in [21], is shown as gray traces in the lower subplot of Figure 9. Multi-objective optimization results for this case study are presented in this section, followed by a discussion on sensitivity of these results to the maximum temperature constraint. The closed-loop graph-based system model takes an average of 35s to simulate for the 30 minute load profile shown in Figure 9, enabling the computationally taxing process of design optimization. The multi-objective optimization problem was formulated and solved using the `gamultiobj` function in the Matlab optimization toolbox [67].

A set of Pareto-optimal designs were obtained by solving the multi-objective HETESS optimization problem. Optimal designs obtained from this study are shown in Figure 8. The Pareto curve obtained from this study shows tradeoffs between the two competing objectives and can be used to inform HETESS design, depending on the desired mass of energy storage elements and desired level of performance. An optimal design was selected from the Pareto curve by qualitatively comparing simulation results from designs on the curve and selecting the design with smallest mass that maintained acceptable performance with respect to each term of the performance cost function (16). In particular, the selected design: i) maintained bus voltage within 1V of the reference; ii) tracked battery power reference without high-amplitude deviations; iii) enforced electronic component temperature constraint violations and maintained CP fluid temperatures less than 2°C above the reference; iv) enforced battery power constraints; v) utilized little pump energy. This design is shown in Figure 8 as a starred point.

18
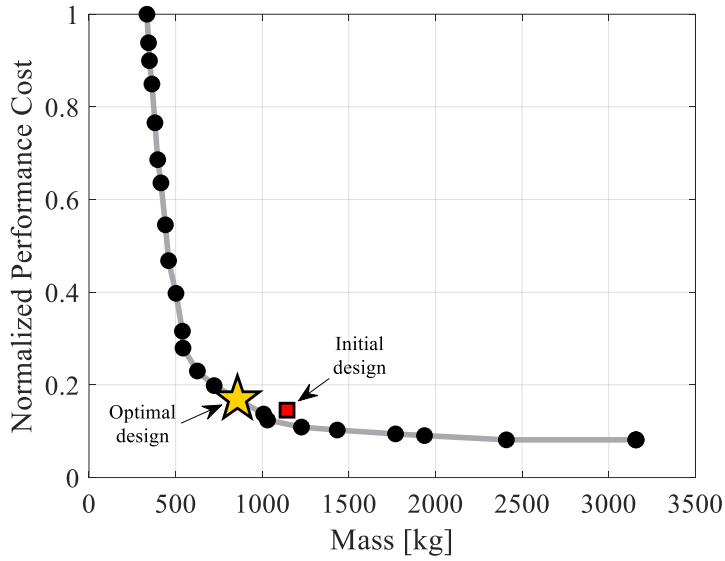
Figure 8: Sizing vs. controller performance Pareto curve.

To evaluate effectiveness of the optimization study, the selected optimal design was compared to the initial HETESS design with nominal design variable values. The initial and optimal values of design variables are provided in the appendix. Comparisons of electrical and thermal trajectories of these designs are shown in Figure 9 and Figure 10. As shown in the upper subplot in Figure 9, the optimal design demonstrates significant improvements in bus voltage reference tracking. In the lower subplot of Figure 9, the optimal design exhibits poorer battery power reference tracking, due to the battery converter duty cycle saturating at its upper limit. This decrease in power tracking performance contributes to a slight increase in the performance cost function for the optimal design. However, the battery is still protected from high discharge rates for the optimal design, which is the goal of the battery converter controller, so these deviations from ideal reference tracking are acceptable. Figure 10 compares thermal trajectories of the initial and optimal designs. The upper subplots plot electronics temperatures of both designs, including mean temperatures of battery cell cores, battery cell surfaces, ultracapacitor cells, power converters, and the simulated load temperature. These subplots show that while electronics are generally cooler for the initial design, their temperatures remain below the 80°C constraint for both designs. The second row of subplots shows less variation in PCM SOCs (solid fractions) for the optimal design. The third row of subplots shows slight improvements in CP temperature reference tracking for the optimal design. Note that trajectories of fluid temperatures through CPs 1 and 2 are nearly identical for the initial design, due in part to the corresponding TES modules having identical melt temperatures. The final row of subplots indicates that flow rates are generally smaller in the optimal design, leading to lower pump energy consumption. Note that flow rates increase towards the end of the simulation as the SOC of PCM1 reaches 0, indicating that the PCM has fully melted. This highlights the utility of PCMs for achieving nearly constant temperatures with low energy consumption. Figure 9 and Figure 10 demonstrate that the final design achieves nearly the same performance as the initial design in terms of the objectives in (16).

Finally, a comparison of initial and optimal HETESS sizing is given in Figure 11. The optimal design is reduced in size by 286 kg – one-fourth of the initial mass of energy storage elements. Comparing masses of each storage element for the initial and optimal designs, battery

19

pack mass is significantly decreased for the optimal design. Ultracapacitor mass is slightly reduced for the optimal design, and PCM mass is increased for the final design. The increase in PCM mass causes the lower variation in PCM SOC noted for the optimal design in Figure 10. By varying amounts of each storage element and optimizing parameters of the controllers, the optimal HETESS design achieves the same level of performance as the initial design with 75% of the original mass.
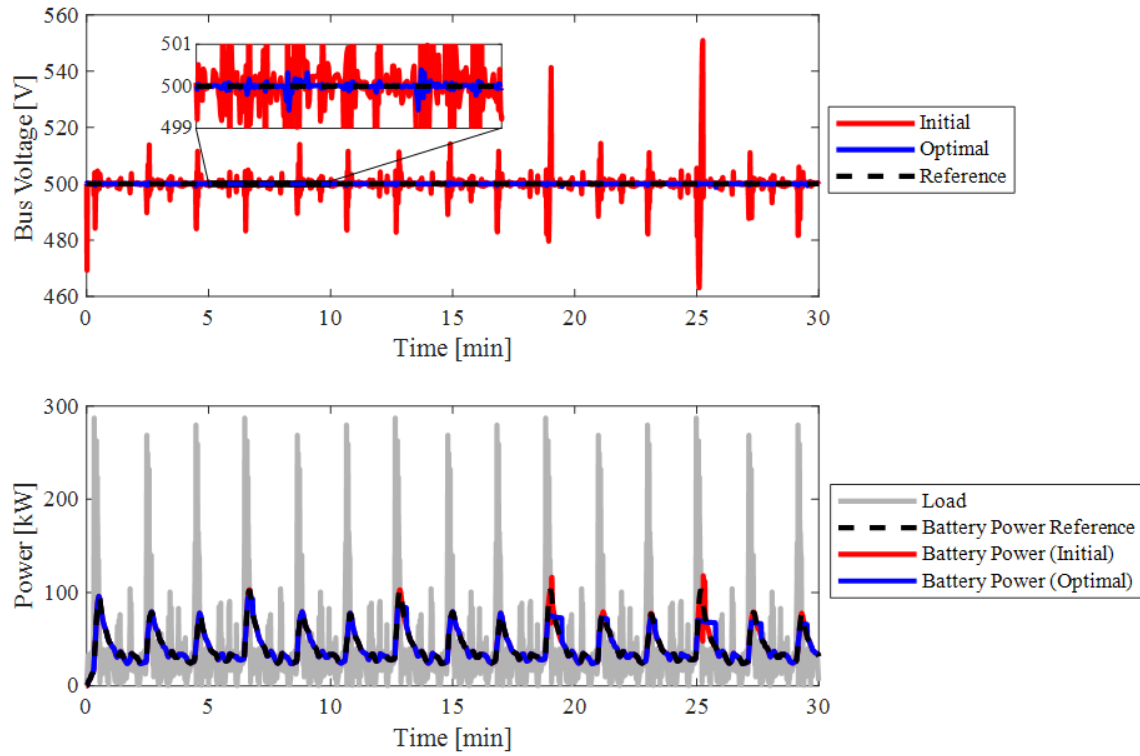
Figure 9: Electrical trajectories of initial and optimal HETESS designs.
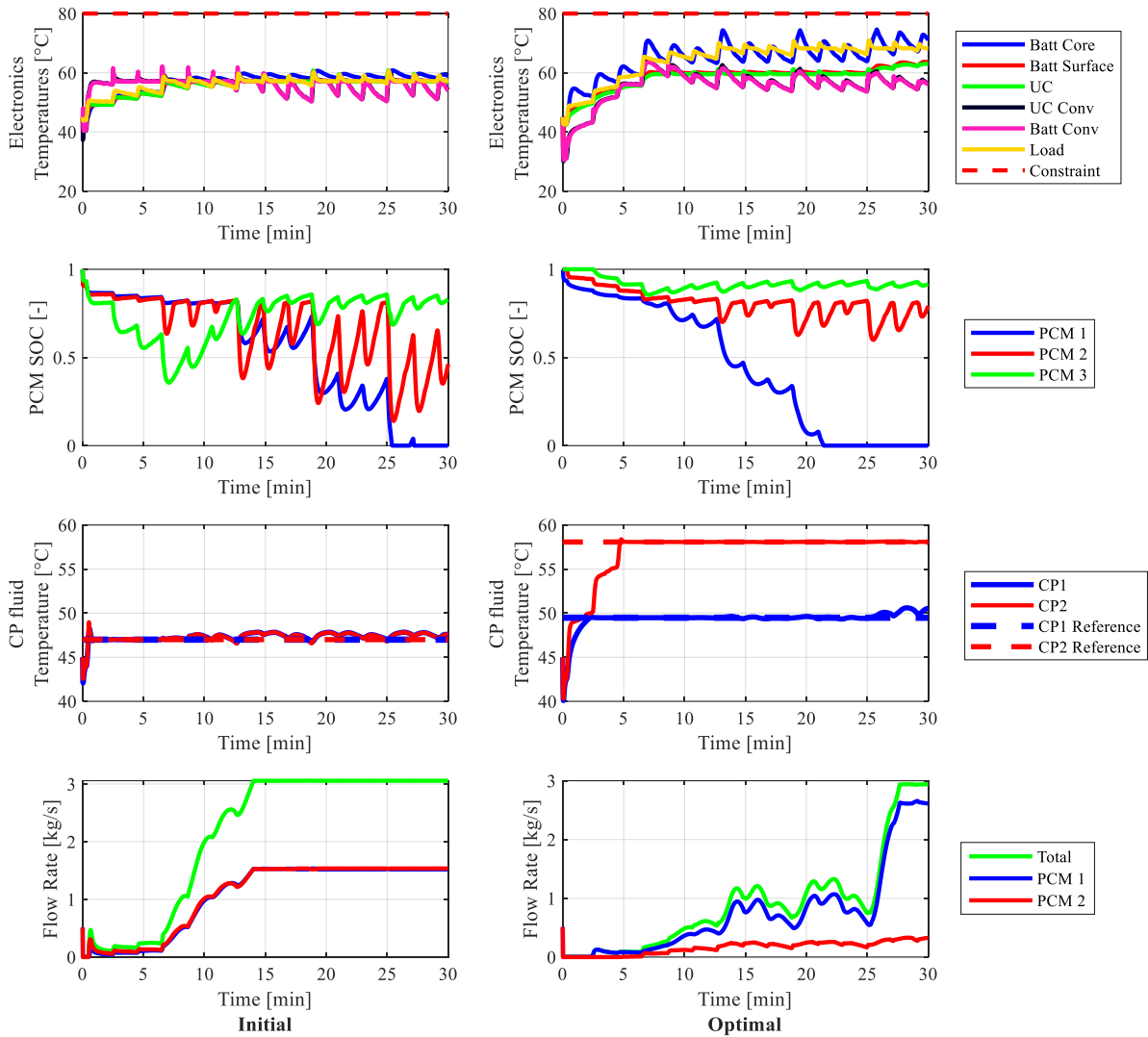
Figure 10: Thermal trajectories of initial (left) and optimal (right) HETESS designs.
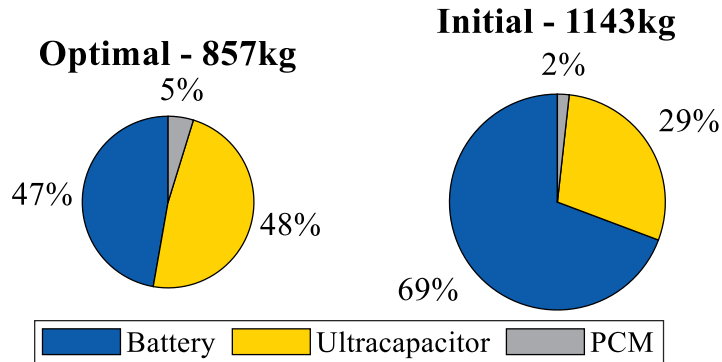

Figure 11: Sizing of initial and optimal HETESS designs.

While electronic component temperatures remain well below the constraint imposed in this case study, temperatures of electrical energy storage components exceed 60°C, which places these components at elevated risks of thermal runaway and accelerated aging [68]. These risks may cause the optimal design identified above to require frequent replacement or repair. As a further example of the benefit and flexibility of the proposed framework, the design optimization column of Figure 2 can be revisited considering lower temperature constraints to mitigate these risks. To explore sensitivity to the temperature constraint, (21) was solved repeatedly for reduced temperature constraints ranging from 35°C to 75°C. Results of this sensitivity study are shown in Figure 12. Figure 12 a) demonstrates a clear trend that lower maximum temperature constraints, especially those below 50°C, exhibit poorer performance in terms of the overall cost described in (16), (17). This trend can be attributed to increased constraint violations and increased pump energy consumption in response to application of tighter constraints. To quantify this trend, the best performance achieved with the lowest temperature constraint is defined as a performance target as shown in Figure 12 a). The mass of energy storage required to meet this target is estimated for each temperature constraint by interpolating between points along respective Pareto fronts. The relationship between these mass estimates, plotted in Figure 12 b), and the respective temperature constraints approximates a power law. This relationship indicates that to achieve the same level of performance as the constraint is reduced from 75°C to 45°C, a 38% mass increase is required. To reduce the constraint from 45°C to 35°C, however, mass required would more than double. These findings provide design insights regarding the tradeoff between performance, mass, and expected thermal stresses to energy storage elements, which would be useful to a system designer.
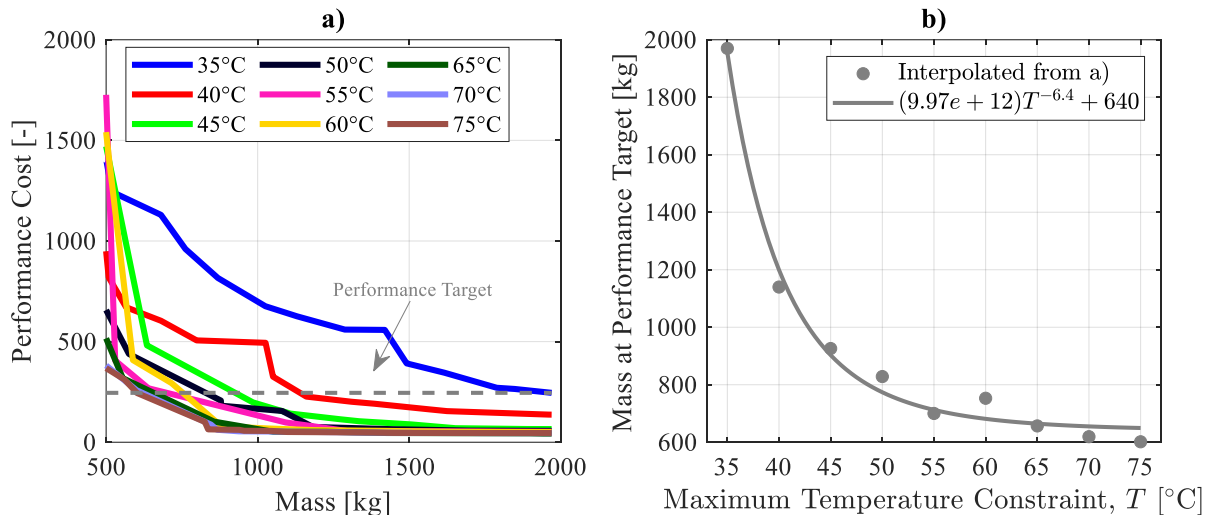

Figure 12: Sensitivity of optimization results to maximum temperature constraint.

5. CONCLUSION

This work provides a graph-based framework for simultaneous design and control optimization of integrated, multi-domain systems. This framework employs modeling tools using graph-theoretic techniques to model energy interactions, allowing users to model a wide range of electro-thermal systems. This framework is flexible in many regards: users can swap component models to capture different behaviors with varying fidelity, configurations can be changed readily, and a suite of different control and design optimization tools can be accommodated to achieve the user's objectives. An HETESS is presented as an example system on which to demonstrate the

22

value of using such a framework for system-level optimization of both plant and controller. A case study is presented in which the framework is used to solve a multi-objective optimization problem for this example system. Results of this case study illustrate the ability to make improvements in multiple objectives (sizing and performance) using the design and control optimization framework. While the HETESS optimization case study is presented to concretely demonstrate its benefits, the framework is broadly applicable to a wide class of electro-thermal systems in a variety of application areas.

Future work will apply advanced control strategies to the HETESS, such as model predictive control. Application of these advanced control strategies in an optimization routine will rely on utilization of more computationally efficient optimization strategies, such as surrogate modeling. Additionally, we note that these validated, low-order component models are subject to deviation from true behavior, so benchtop testing of optimal system designs generated by the optimization framework can verify the validity of the system model used for optimization.

CONFLICT OF INTEREST

The authors declare that they have no conflict of interest.

ACKNOWLEDGEMENTS

APPENDIX

Table 4: Initial and optimal design variable values.

Plant Design Variable	Initial	Optimal	Controller Design Variable	Initial	Optimal
Parallel battery cells	40	20	α_1^{HESS}	1	8.03
Series UC cells	320	468	β_1^{HESS}	1	8.41
Parallel UC cells	45	38	α_2^{HESS}	1	7.97
PCM1 mass [kg]	10	16.2	β_2^{HESS}	1	5.97
PCM1 melt temperature [°C]	57	59	α_1^{TESS}	1	3.66
PCM2 mass [kg]	5	11.4	β_1^{TESS}	1	4.21
PCM2 melt temperature [°C]	57	68	α_2^{TESS}	1	4.95
PCM3 mass [kg]	5	13.3	β_2^{TESS}	1	8.76
PCM3 melt temperature [°C]	57	70	-	-	-

REFERENCES

[1]   A. Runge-Metzger, "A Clean Planet for all. A European long-term strategic vision for a prosperous, modern, competitive and climate neutral economy," Brussels, 2018.

[2]   S. L. Myers, "China's Pledge to Be Carbon Neutral by 2060: What It Means," *The New York Times*, Sep. 23, 2020. [Online]. Available: https://www.nytimes.com/2020/09/23/world/asia/china-climate-change.html

[3]   International Energy Agency, "Global EV Outlook 2020," OECD, Jun. 2020. doi: 10.1787/d394399e-en.

[4]   U.S. Department of Energy, "Electrical and Electronics Technical Team Roadmap," *U.S. DRIVE Partnership*, 2017, [Online]. Available: https://www.energy.gov/sites/prod/files/2017/11/f39/EETT Roadmap 10-27-17.pdf

[5]   K. Rajashekara, "Present status and future trends in electric vehicle propulsion technologies," *IEEE J. Emerg. Sel. Top. Power Electron.*, vol. 1, no. 1, pp. 3–10, 2013, doi: 10.1109/JESTPE.2013.2259614.

[6]   T. Mahefkey, K. Yerkes, B. Donovan, and M. Ramalingam, "Thermal Management Challenges For Future Military Aircraft Power Systems," *SAE J. Aerosp.*, vol. 113, 2004, doi: https://doi.org/10.4271/2004-01-3204.

[7]   F. Un-Noor, S. Padmanaban, L. Mihet-Popa, M. N. Mollah, and E. Hossain, "A comprehensive study of key electric vehicle (EV) components, technologies, challenges, impacts, and future direction of development," *Energies*, vol. 10, no. 8, 2017, doi: 10.3390/en10081217.

[8]   J. R. R. A. Martins and A. B. Lambe, "Multidisciplinary design optimization: A survey of architectures," *AIAA J.*, vol. 51, no. 9, pp. 2049–2075, Sep. 2013, doi: 10.2514/1.J051895.

[9]   M. Garcia-Sanz, "Control Co-Design: An engineering game changer," *Adv. Control Appl. Eng. Ind. Syst.*, vol. 1, no. 1, Dec. 2019, doi: 10.1002/adc2.18.

[10]   J. T. Allison and D. R. Herber, "Multidisciplinary design optimization of dynamic engineering systems," *54th AIAA/ASME/ASCE/AHS/ASC Structures, Structural Dynamics, and Materials Conference*, 2013. doi: 10.2514/6.2013-1462.

[11]   R. Hemmati and H. Saboori, "Emergence of hybrid energy storage systems in renewable energy and transport applications – A review," *Renew. Sustain. Energy Rev.*, vol. 65, pp. 11–23, Nov. 2016, doi: 10.1016/j.rser.2016.06.029.

[12]   R. Xiong, H. Chen, C. Wang, and F. Sun, "Towards a smarter hybrid energy storage system based on battery and ultracapacitor - A critical review on topology and energy management," *J. Clean. Prod.*, vol. 202, pp. 1228–1240, Nov. 2018, doi: 10.1016/j.jclepro.2018.08.134.

[13]   A. Ostadi, M. Kazerani, and S. K. Chen, "Hybrid Energy Storage System (HESS) in vehicular applications: A review on interfacing battery and ultra-capacitor units," *IEEE Transportation Electrification Conference and Expo*, 2013, doi: 10.1109/ITEC.2013.6573471.

[14]   J. P. Zheng, T. R. Jow, and M. S. Ding, "Hybrid power sources for pulsed current applications," *IEEE Trans. Aerosp. Electron. Syst.*, vol. 37, no. 1, pp. 288–292, 2001, doi: 10.1109/7.913688.

[15]   A. Kuperman and I. Aharon, "Battery-ultracapacitor hybrids for pulsed current loads: A review," *Renew. Sustain. Energy Rev.*, vol. 15, no. 2, pp. 981–992, 2011, doi: 10.1016/j.rser.2010.11.010.

[16]   C. E. Laird and A. G. Alleyne, "A hybrid electro-thermal energy storage system for high

ramp rate power applications," *Dynamic Systems and Control Conference*, 2019. doi: 10.1115/DSCC2019-9089.

[17] C. B. Baxi and T. Knowles, "Thermal energy storage for solid-state laser weapons systems," *J. Dir. Energy*, vol. 1, no. 4, pp. 293–308, 2006.

[18] H. C. Pangborn, C. E. Laird, and A. G. Alleyne, "Hierarchical Hybrid MPC for Management of Distributed Phase Change Thermal Energy Storage," *American Control Conference*, 2020. doi: 10.23919/ACC45564.2020.9147698.

[19] Z. Song, H. Hofmann, J. Li, X. Han, and M. Ouyang, "Optimization for a hybrid energy storage system in electric vehicles using dynamic programing approach," *Appl. Energy*, vol. 139, pp. 151–162, Feb. 2015, doi: 10.1016/j.apenergy.2014.11.020.

[20] X. Hu, L. Johannesson, N. Murgovski, and B. Egardt, "Longevity-conscious dimensioning and power management of the hybrid energy storage system in a fuel cell hybrid electric bus," *Appl. Energy*, vol. 137, pp. 913–924, Jan. 2015, doi: 10.1016/j.apenergy.2014.05.013.

[21] J. Liu, H. Dong, T. Jin, L. Liu, B. Manouchehrinia, and Z. Dong, "Optimization of Hybrid Energy Storage Systems for Vehicles with Dynamic On-Off Power Loads Using a Nested Formulation," *Energies*, vol. 11, no. 10, 2018, doi: 10.3390/en11102699.

[22] H. H. Eldeeb, A. T. Elsayed, C. R. Lashway, and O. Mohammed, "Hybrid Energy Storage Sizing and Power Splitting Optimization for Plug-In Electric Vehicles," *IEEE Trans. Ind. Appl.*, vol. 55, no. 3, pp. 2252–2262, May 2019, doi: 10.1109/TIA.2019.2898839.

[23] R. E. Araújo, R. De Castro, C. Pinto, P. Melo, and D. Freitas, "Combined sizing and energy management in EVs with batteries and supercapacitors," *IEEE Trans. Veh. Technol.*, vol. 63, no. 7, pp. 3062–3076, Sep. 2014, doi: 10.1109/TVT.2014.2318275.

[24] P. Saenger, N. Devillers, K. Deschinkel, M. C. Pera, R. Couturier, and F. Gustin, "Optimization of Electrical Energy Storage System Sizing for an Accurate Energy Management in an Aircraft," *IEEE Trans. Veh. Technol.*, vol. 66, no. 7, pp. 5572–5583, 2017, doi: 10.1109/TVT.2016.2617288.

[25] A. Al Mamun, Z. Liu, D. M. Rizzo, and S. Onori, "An integrated design and control optimization framework for hybrid military vehicle using lithium-ion battery and supercapacitor as energy storage devices," *IEEE Trans. Transp. Electrif.*, vol. 5, no. 1, pp. 239–251, 2019, doi: 10.1109/TTE.2018.2869038.

[26] J. Shen, S. Dusmez, and A. Khaligh, "Optimization of sizing and battery cycle life in battery/ultracapacitor hybrid energy storage systems for electric vehicle applications," *IEEE Trans. Ind. Informatics*, vol. 10, no. 4, pp. 2112–2121, 2014, doi: 10.1109/TII.2014.2334233.

[27] J. Shen, A. Hasanzadeh, and A. Khaligh, "Optimal power split and sizing of hybrid energy storage system for electric vehicles," *IEEE Transportation Electrification Conference and Expo*, 2014. doi: 10.1109/itec.2014.6861861.

[28] S. Wen *et al.*, "Optimal sizing of hybrid energy storage sub-systems in PV/diesel ship power system using frequency analysis," *Energy*, vol. 140, pp. 198–208, 2017, doi: 10.1016/j.energy.2017.08.065.

[29] Z. Song, J. Hou, S. Xu, M. Ouyang, and J. Li, "The influence of driving cycle characteristics on the integrated optimization of hybrid energy storage system for electric city buses," *Energy*, vol. 135, pp. 91–100, Sep. 2017, doi: 10.1016/j.energy.2017.06.096.

[30] N. Javani, I. Dincer, G. F. Naterer, and B. S. Yilbas, "Exergy analysis and optimization of a thermal management system with phase change material for hybrid electric vehicles,"

Appl. Therm. Eng., vol. 64, no. 1–2, pp. 471–482, Mar. 2014, doi: 10.1016/j.applthermaleng.2013.11.053.

[31]   S. M. Aceves, H. Nakamura, G. M. Reistad, and J. Martinez-Frias, "Optimization of a class of latent thermal energy storage systems with multiple phase-change materials," *J. Sol. Energy Eng.*, vol. 120, no. 1, pp. 14–19, Feb. 1998, doi: 10.1115/1.2888040.

[32]   A. Stupar, U. Drofenik, and J. W. Kolar, "Optimization of phase change material heat sinks for low duty cycle high peak load power supplies," *IEEE Trans. Components, Packag. Manuf. Technol.*, vol. 2, no. 1, pp. 102–115, Jan. 2012, doi: 10.1109/TCPMT.2011.2168957.

[33]   D. Kong, R. Peng, P. Ping, J. Du, G. Chen, and J. Wen, "A novel battery thermal management system coupling with PCM and optimized controllable liquid cooling for different ambient temperatures," *Energy Convers. Manag.*, vol. 204, Jan. 2020, doi: 10.1016/j.enconman.2019.112280.

[34]   V. Shanmugasundaram, J. R. Brown, and K. L. Yerkes, "Thermal management of high heat-flux sources using phase change materials: A design optimization procedure," *32nd Thermophysics Conference*, 1997. doi: 10.2514/6.1997-2451.

[35]   G. P. Henze, R. H. Dodier, and M. Krarti, "Development of a predictive optimal controller for thermal energy storage systems," *HVAC&R Res.*, vol. 3, no. 3, pp. 233–264, 1997, doi: 10.1080/10789669.1997.10391376.

[36]   Y. Ma, A. Kelman, A. Daly, and F. Borrelli, "Predictive control for energy efficient buildings with thermal storage: Modeling, simulation, and experiments," *IEEE Control Syst. Mag.*, vol. 32, no. 1, pp. 44–64, 2012, doi: 10.1109/MCS.2011.2172532.

[37]   J. A. Candanedo, V. R. Dehkordi, and M. Stylianou, "Model-based predictive control of an ice storage device in a building cooling system," *Appl. Energy*, vol. 111, pp. 1032–1045, Nov. 2013, doi: 10.1016/j.apenergy.2013.05.081.

[38]   H. Mehrjerdi and E. Rakhshani, "Optimal operation of hybrid electrical and thermal energy storage systems under uncertain loading condition," *Appl. Therm. Eng.*, vol. 160, Sep. 2019, doi: 10.1016/j.applthermaleng.2019.114094.

[39]   A. Baniasadi, D. Habibi, W. Al-Saedi, M. A. S. Masoum, C. K. Das, and N. Mousavi, "Optimal sizing design and operation of electrical and thermal energy storage systems in smart buildings," *J. Energy Storage*, vol. 28, Apr. 2020, doi: 10.1016/j.est.2019.101186.

[40]   M. Giuntoli and D. Poli, "Optimized thermal and electrical scheduling of a large scale virtual power plant in the presence of energy storages," *IEEE Trans. Smart Grid*, vol. 4, no. 2, pp. 942–955, 2013, doi: 10.1109/TSG.2012.2227513.

[41]   T. Li, H. Liu, and D. Ding, "Predictive energy management of fuel cell supercapacitor hybrid construction equipment," *Energy*, vol. 149, pp. 718–729, Apr. 2018, doi: 10.1016/j.energy.2018.02.101.

[42]   M. Valenzuela Guzman and M. A. Valenzuela, "Integrated mechanical-electrical modeling of an AC electric mining shovel and evaluation of power requirements during a truck loading cycle," *IEEE Trans. Ind. Appl.*, vol. 51, no. 3, pp. 2590–2599, 2015, doi: 10.1109/TIA.2014.2375378.

[43]   T. Zimmermann, P. Keil, M. Hofmann, M. F. Horsche, S. Pichlmaier, and A. Jossen, "Review of system topologies for hybrid electrical energy storage systems," *J. Energy Storage*, vol. 8, pp. 78–90, 2016, doi: 10.1016/j.est.2016.09.006.

[44]   C. T. Aksland, "Modular Modeling And Control of A Hybrid Unmanned Aerial Vehicle's Powertrain," MS Thesis, University of Illinois at Urbana-Champaign, 2019.

[45] M. A. Williams, J. P. Koeln, H. C. Pangborn, and A. G. Allenye, "Dynamical Graph Models of Aircraft Electrical, Thermal, and Turbomachinery Components," *J. Dyn. Syst. Meas. Control*, vol. 140, no. 4, pp. 1–17, 2018, doi: 10.1115/1.4038341.

[46] J. P. Koeln, M. A. Williams, H. C. Pangborn, and A. G. Alleyne, "Experimental validation of graph-based modeling for thermal fluid power flow systems," *Dynamic Systems and Control Conference*, 2016. doi: 10.1115/DSCC2016-9782.

[47] J. P. Koeln, "Hierarchical Power Management in Vehicle Systems," PhD Dissertation, University of Illinois at Urbana-Champaign, 2016.

[48] D. J. Docimo and A. G. Alleyne, "Electro-Thermal Graph-Based Modeling for Hierarchical Control with Application to an Electric Vehicle," *IEEE Conference on Control Technology and Applications*, 2018. doi: 10.1109/CCTA.2018.8511390.

[49] H. C. Pangborn, J. P. Koeln, M. A. Williams, and A. G. Alleyne, "Experimental validation of graph-based hierarchical control for thermal management," *J. Dyn. Syst. Meas. Control*, vol. 140, no. 10, pp. 1–16, 2018, doi: 10.1115/1.4040211.

[50] H. C. Pangborn, "Hierarchical control for multi-domain coordination of vehicle energy systems with switched dynamics," PhD Dissertation, University of Illinois at Urbana-Champaign, 2019. Accessed: Sep. 03, 2019. [Online]. Available: https://www.ideals.illinois.edu/handle/2142/104799

[51] C. T. Aksland and A. G. Alleyne, "Hierarchical model-based predictive controller for a hybrid UAV powertrain," *Control Eng. Pract.*, vol. 115, no. November 2020, p. 104883, 2021, doi: 10.1016/j.conengprac.2021.104883.

[52] C. T. Aksland, T. W. Bixel, L. C. Raymond, M. A. Rottmayer, and A. G. Alleyne, "Graph-based electro-mechanical modeling of a hybrid unmanned aerial vehicle for real-time applications," *Proc. Am. Control Conf.*, vol. 2019-July, pp. 4253–4259, 2019.

[53] K. M. Russell, C. T. Aksland, and A. G. Alleyne, "Graph-Based Dynamic Modeling of Two-Phase Heat Exchangers in Vapor Compression Systems," *Int. J. Refrig.*, 2022.

[54] C. Laird, "Modeling, control, and design of hybrid electrical and thermal energy storage systems," MS Thesis, University of Illinois at Urbana-Champaign, 2021.

[55] P. D. Silva, L. C. Gonçalves, and L. Pires, "Transient behaviour of a latent-heat thermal-energy store: Numerical and experimental studies," *Appl. Energy*, vol. 73, no. 1, pp. 83–98, 2002, doi: 10.1016/S0306-2619(02)00060-0.

[56] M. A. Williams, "A framework for the control of electro-thermal aircraft power systems," PhD Dissertation, University of Illinois at Urbana-Champaign, 2017. Accessed: Feb. 27, 2021. [Online]. Available: https://www.ideals.illinois.edu/handle/2142/99285

[57] J. P. Koeln, H. C. Pangborn, M. A. Williams, M. L. Kawamura, and A. G. Alleyne, "Hierarchical Control of Aircraft Electro-Thermal Systems," *IEEE Trans. Control Syst. Technol.*, pp. 1–15, 2019, doi: 10.1109/tcst.2019.2905221.

[58] D. J. Docimo, H. C. Pangborn, and A. G. Alleyne, "Hierarchical control for electro-thermal power management of an electric vehicle powertrain," *ASME 2018 Dyn. Syst. Control Conf. DSCC 2018*, vol. 2, pp. 1–10, 2018, doi: 10.1115/DSCC2018-9215.

[59] Z. Li, O. Onar, A. Khaligh, and E. Schaltz, "Design, control, and power management of a battery/ultra-capacitor hybrid system for small electric vehicles," *SAE Technical Papers*, 2009. doi: 10.4271/2009-01-1387.

[60] Y. Peng, D. Vrancic, and R. Hanus, "Anti-Windup, Bumpless, and Conditioned Transfer Techniques for PID Controllers," *IEEE Control Syst. Mag.*, vol. 16, no. 4, pp. 48–57, 1996.

[61] RubiTherm, "PCM RT-Line." https://www.rubitherm.eu/en/index.php/productcategory/organische-pcm-rt

[62] ExxonMobil, "Parvan - Fully Refined Paraffin Wax." https://www.exxonmobil.com/en/wax/fully-refined-paraffin-wax

[63] Axiotherm, "Axiotherm PCM - products." https://www.axiotherm.de/en/produkte/axiotherm-pcm/ (accessed Apr. 20, 2022).

[64] D. J. Docimo, Z. Kang, K. A. James, and A. G. Alleyne, "A Novel Framework for Simultaneous Topology and Sizing Optimization of Complex, Multi-Domain Systems-of-Systems," *J. Mech. Des.*, vol. 142, pp. 1–37, 2020, doi: 10.1115/1.4046066.

[65] W. H. Press, S. A. Teukolsky, W. T. Vetterling, and B. P. Flannery, *Numerical recipes: the art of scientific computing*, 3rd ed. Cambridge, UK: Cambridge University Press, 2007.

[66] D. Docimo, Z. Kang, K. James, and A. Alleyne, "Plant and Controller Optimization for Power and Energy Systems with Model Predictive Control," *J. Dyn. Syst. Meas. Control*, Mar. 2021, doi: 10.1115/1.4050399.

[67] K. Deb, *Multi-objective optimization using evolutionary algorithms*. Chichester ; John Wiley & Sons, 2001.

[68] S. Ma *et al.*, "Temperature effect and thermal impact in lithium-ion batteries: A review," *Prog. Nat. Sci. Mater. Int.*, vol. 28, no. 6, pp. 653–666, 2018, doi: 10.1016/j.pnsc.2018.11.002.